COMPARATIVE STUDY OF FREQUENCY DEPENDENCY IN HIGH RESOLUTION SONAR IMAGERY FROM THE MANEX'13 SEA TRIALS

Marc Geilhufe Norwegian Defence Research Establishment (FFI), Kjeller, Norway
Samantha Dugelay Centre for Maritime Research and Experimentation (CMRE), La Spezia, Italy
Stig A. V. Synnes Norwegian Defence Research Establishment (FFI), Kjeller, Norway
Torstein O. Sæbø Norwegian Defence Research Establishment (FFI), Kjeller, Norway
Øivind Midtgaard Norwegian Defence Research Establishment (FFI), Kjeller, Norway
Roy E. Hansen Norwegian Defence Research Establishment (FFI), Kjeller, Norway

Email: marc.geilhufe@ffi.no

1 INTRODUCTION

MANEX'13 (Multi-national Autonomy Experiment 2013)[1] was organized by the Centre for Maritime Research and Experimentation (CMRE), a NATO Science and Technology Organization, and run from the NATO research vessel (NRV) Alliance off the island of Elba in Italy. The Norwegian Defence Research Establishment (FFI) and CMRE conducted a side experiment to gather centimeter resolution sonar imagery of seafloor and targets engaging three different autonomous underwater vehicles (AUVs) with acoustic imaging capability on four different frequency bands. These AUVs and sensor systems were: FFI's HUGIN-HUS AUV with HISAS synthetic aperture sonar (SAS) covering 12 – 38 kHz and 60 – 85 kHz, CMRE's MUSCLE AUV with MUSCLE SAS covering 270 – 330 kHz and CMRE's REMUS100 AUV with a Marine Sonic side-scan sonar (SSS) centered at 900 kHz. Due to acoustic interference, only the lower part of the low frequency HISAS band was valid (i.e., 12 – 25 kHz). The AUV systems were run on the same survey lines, with additional intermediary lines for the REMUS100 accounting for its shorter recording range.

The acoustic frequencies used in a sonar system will affect the sonar images in many ways. All terms in the sonar equation (the energy conservation equation) are dependent of the frequency[2]. Noticeably, the transmission loss is frequency dependent in such a way that higher frequencies have more limited range, and the backscattered signal strength is in general frequency dependent. In side-scan sonar, the along-track resolution is frequency dependent. In SAS, the image resolution is independent of frequency, while the image quality and the information content is not[3].

In this study we present examples of the recorded high resolution imagery and give a comparative study of the frequency dependency. The paper is not focused towards comparing models with data, but rather to show differences in sonar imagery that might be related to the acoustic frequency used. Due to practical limitations given by the data collected, we were not able to do a full analysis of all the relevant frequency dependencies. In particular, the sonar images are taken with side-looking systems at relatively small grazing angles.

Section 2 gives a brief review of basic scattering theory and related work. In Section 3 we present information about the MANEX'13 sea trials, the AUV systems and the setup of the frequency comparison. Frequency dependent aspects of example imagery are discussed broadly in Section 4 before a preliminary statistical analysis of homogeneous seabed types on corresponding image snippets of HUGIN-HUS and MUSCLE is performed in Section 5. The final Section 6 summarizes this paper and gives ideas for future work.

2 SEAFLOOR SCATTERING

Seafloor scattering can be expressed by a composite model containing a surface scattering component and a volume scattering component (where the latter incorporates bottom penetration)[4]. The contribution of both components changes with seafloor type, geometry, and with frequency. Model parameters have been determined quite successfully for a range of seafloor types, incident angles and frequencies through fitting with empirical measurements in models such as the Jackson scattering model[5]. The surface scattering for side-looking geometry of SAS and SSS is typically limited to diffuse scattering (excluding specular scattering).

Object scattering also have similar surface and volume scattering components. Both surface-bottom scattering and internal volume scattering will be affected by the observation angle, the orientation of the object on the seafloor and whether the object is buried[6]. When observing objects from different aspects, the scattering may contain a specular component with higher scattering strength. The volume scattering can be dominated by the internal structure at low frequencies with more penetration into the object, where resonances and elasticity of the objects can be important for many objects[7].

In order to perform a proper analysis, the sonar hardware and signal processing should be energy preserving, such that absolute calibrated images with a direct measure of target strength could be provided. However, as the addressed systems are not calibrated, this study is limited to relative scattering strengths within each band. Next, the images should have comparable geometrical resolution both in the along-track and the across-track direction. We obtain a fixed along-track resolution by adopting a (synthetic) aperture length that is increasing inversely proportional to the acoustic frequency[8]. Longer aperture at lower frequencies leads to integration of a wider range of look angles on the object, resulting in shadow fill-in[9] and a higher probability of including specular reflection[8]. Specular reflection could be separated through multi-aspect imaging at lower resolution[10].

There are several different effects that might cause frequency dependencies in the sonar image: The scattering strength could have scale dependence in the rough surface; the volume penetration and the sediment scattering is frequency dependent; the reflection coefficient might be frequency dependent; for objects, there could be specific resonance frequencies; the shadow from objects is affected by angular spread which is frequency dependent; there will be increased occurrence of specular reflections by increased angular spread.

Related work include the SAX'99 (Sediment Acoustics Experiment 1999). The trial focused on quantifying backscattering from the seafloor sediment, penetration into the sediment, and propagation within the sediment. In addition, spheres and other objects were used to gather data on acoustic detection of buried objects[11]. The applied sonar operated in frequency bands of 15 – 25 kHz and 165 – 195 kHz[10]. In 2002, the system was upgraded with an additional 8 – 55 kHz broadband sensor[12] and was used in SAX'04[13]. Results from the trials suggest that the highest frequencies provide no bottom penetration and images only proud targets. The lowest frequencies will penetrate the sea bottom for a few centimeters and provide images of buried objects[9,14]. An approach for target classification was suggested, where each object in the SAS images is isolated before the average scattering strength versus frequency (using sub-band processing) and look angle is investigated[15]. In[16], automated detection on high resolution SAS imagery on two and three frequency bands showed improved performance versus operating on a single band.

3 MANEX'13 SEA TRIALS

3.1 General facts

The MANEX'13 sea trials were conducted from CMRE's research vessel Alliance off the island of Elba (see Fig. 1), Italy, from September 30th to October 25th 2013, and included participants from nine nations[1]. Although the primary aim of the trial was to test and demonstrate novel concepts and technologies for autonomous mine hunting, it also provided a rare opportunity for recording coordinated data from sonar systems operating at widely separated frequencies. In this study, we have used sensor data collected with three different AUVs: FFI's HUGIN-HUS as well as CMRE's MUSCLE and REMUS100 (see right column of Fig. 1).

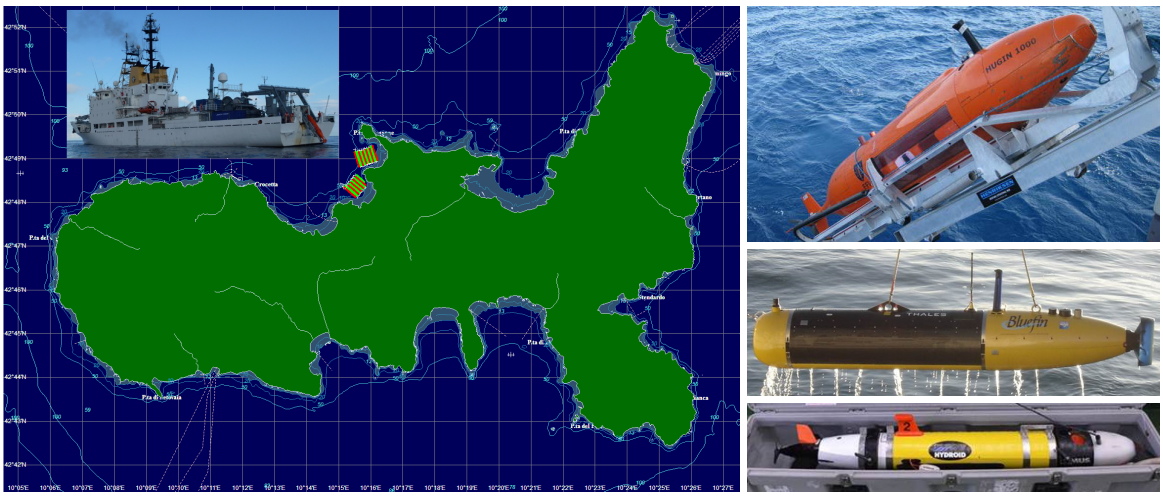

Figure 1: *Left: NRV Alliance with the HUGIN-HUS AUV during the MANEX'13 trials overlaid on map of the Italian island Elba highlighting the two common survey areas (green and red stripes in the north of the island). Right: AUV's from top to bottom: HUGIN-HUS, MUSCLE, REMUS100.*

The HUGIN AUV has been developed by Kongsberg Maritime and FFI. HUGIN-HUS has a diameter of 75 cm and is equipped with HISAS 1030[17], which is an interferometric SAS that generates high-resolution imagery and bathymetry of the seafloor. HISAS usually operates with a 30 kHz frequency band centered at 100 kHz, and a nominal range of 200 m to each side for a platform speed of 2 m/s. On HUGIN-HUS, however, an additional low frequency transmitter has been mounted and the high frequency band has been extended down to 60 kHz[8]. This configuration allows experimentation with various frequency modes. In this study we used a combined mode with simultaneous frequency bands 12 – 38 kHz (further referred to as LF) and 60 – 85 kHz (further referred to as MF) with a data recording range of 92 m. The Tilefish optical camera system is a prototype developed for the HUGIN-HUS AUV through a co-operation between Norsk Elektro Optikk and FFI. It consists of a high-resolution, high sensitivity digital still image camera and a synchronized strobe with multiple blue-green light emitting diodes (LED).

The MUSCLE system[18] is a Thales Underwater Systems SAS mounted on a Bluefin AUV (3.5 m long, diameter 0.53 m). The SAS processing software has been developed by CMRE and is implemented using graphics processing units (GPUs) for delayed real-time processing within the vehicle. MUSCLE features a sonar range of 150 m at a carrier frequency of 300 kHz.

The REMUS100, developed by Hydroid, is a smaller AUV (1.6 m long, diameter 0.19 m), which has a depth rating of 100 m. The CRME version is equipped with Marine Sonic SSS[19] operating at 900 or 1800 kHz having variable sonar ranges with an average maximum range of 40 m (for 900 kHz) or 15 m (for 1800 kHz) respectively. The data is recorded in 512 samples per ping and channel. In this study the maximum range is set to 30 m.

3.2 Comparative frequency study

For this study, we have recorded data in Biodola bay and Viticcio bay on the north side of Elba. Their geographic locations are highlighted in the map of Elba in Fig. 1, where Viticcio bay is located northeast of Biodola. Table 1 gives an overview of the recorded frequencies, effective slant range interval, pixel size, resolution and the survey dates for all three AUV systems. In order to make the comparison as realistic as possible, common waypoints were determined for both bays such that HUGIN-HUS and MUSCLE could record sonar data on basically equal survey lines that only differ slightly due to smaller navigation inaccuracies. Because of a shorter recording range, intermediate lines had to be used for REMUS100. Thus the geometry in form of grazing angle and target range is different, and depending on the observed area of interest the heading and side of REMUS100 can be opposite to those from the HUGIN-HUS and MUSCLE runs.

Example imagery from the same scenes recorded by the three different systems are shown in Fig. 2. Sonar images in columns 1, 2 and 4 are displayed on a 20x20 m grid whilst the displayed area is 25x25 m in the third column. The first column exhibits a 75 cm long diver bag on smooth sediment to

Table 1: *Overview of the different sonar systems properties used in this study*

	HUGIN-HUS HISAS LF & MF	MUSCLE	REMUS100 Marine Sonic
Frequency	12 – 38 kHz (LF)* 60 – 85 kHz (MF)	270 – 330 kHz	900 kHz
Slant range interval	15 – 72.5 m (LF) 5.5 – 77.5 m (MF)	40 – 150 m	5 – 30 m
Pixel size (range x along-track)	2.0 x 2.0 cm	1.5 x 2.5 cm	5.9 x 12 cm
Resolution (range x along-track)	5.9 x 2.6 cm (LF)* 3.1 x 2.8 cm (MF)	1.5 x 2.5 cm	range dependent
Survey date Biodola bay	October 12, 2013	October 9, 2013	October 7, 2013
Survey date Viticcio bay	October 13, 2013	October 2, 2013	October 4, 2013

*Due to interference, only the lower half of the frequency band (12 – 25 kHz) was used in this study, effectively degrading the theoretical across-track resolution to 5.9 cm.

display frequency dependent target responses, while the other columns depict a flat sandy seabed with a large section of cable, a seabed of Posidonia interspersed with sandy zones and a denser Posidonia area. Corresponding optical Tilefish camera images cover approximately 3.5x3.5 m and were obtained at an altitude of 8 – 9 m with pixel size around 6 mm. In the third column, the optical image is not part of the displayed scene due to lack of data. It is obtained from few meters nearby, where we believe that the seafloor shows comparable features. Note that there are some differences between the two types of images. For instance, the patches of Posidonia appear brighter than the surrounding sediment seafloor in the sonar image, while the opposite is observed for the optical images. A qualitative investigation of the frequency dependence in Fig. 2 follows in Section 4 and a statistical analysis of the latter three columns in Fig. 2 will be performed in Section 5.

4 QUALITATIVE INVESTIGATION

In this section we discuss qualitative differences in the data presented in Fig. 2 and relate it to geometry and frequency dependence from simple scattering theory. One main acoustic frequency dependent property in sonar imaging is penetration[4]. Low frequencies penetrate more into seafloor and objects than high frequencies. This causes two main effects in sonar images: Firstly, at low frequencies a sonar image will reveal more of the seafloor sediment structure, while at high frequencies the image will give a clearer representation of the actual seafloor surface. This effect can be seen in the left column of Fig. 2. In the LF images at the top row, the underlying sediment structure can be clearly seen. In the panels from top to bottom the frequency increases and the sediment structure gradually disappears.

Another effect caused by frequency dependent penetration is that objects may appear very differently. For high frequencies, the acoustic signals do not penetrate into the object and the echo directly represents the outer shape of the object. For lower frequencies, the signal may penetrate into the object and show internal structure or even penetrate directly through the object. This effect is not very clear in the example images in Fig. 2, but the 300 kHz image of the diver bag (in the left column) has a highlight with a shape that looks more like a diver bag than the highlight in the 18.5 kHz image. In the 900 kHz image, the resolution is too poor to make out the shape of the highlight.

In SAS imaging the theoretical along-track resolution is frequency independent. This is achieved by increasing the length of the synthetic aperture inversely proportional to the frequency[3]. This means that the observation geometry is frequency dependent, which leads to two main effects in the images: Firstly, shadow behind objects will be blurred at the edges and partly filled in at low frequencies due to the wider observation angles. The sharpest shadow edges are achieved by using conventional side-scan sonar like the Marine Sonic, except in the cases where the resolution is too poor to resolve the shadow. The images of the diver bag in the left column of Fig. 2, shows that the shadow gradually disappears at low frequencies. The other geometry dependent effect is

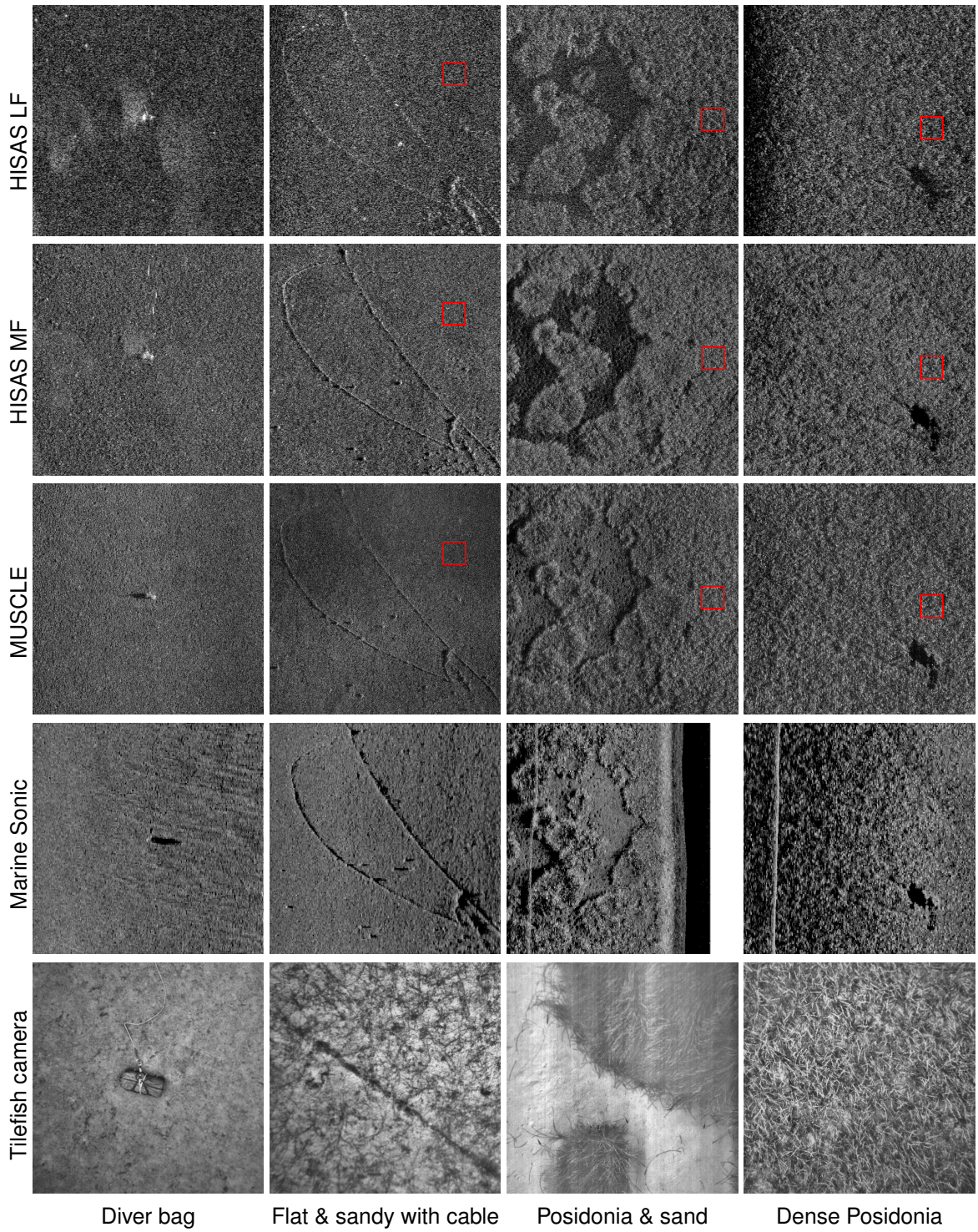

Figure 2: *SAS images from HUGIN-HUS (HISAS LF and MF) and MUSCLE as well as SSS images from REMUS100 (Marine Sonic) and optical images for parts of the given seafloor. The red boxes superimposed on the images corresponds roughly to the patch of homogeneous seabed used for statistical comparison in Section 5.*

that for low frequencies with a broad selection of observation angles, it is more likely that an object will give a specular reflection. Since a specular reflection is very strong relative to non-specular scattering, an object may have a stronger highlight in a low frequency image relative to higher frequencies. This effect can be seen in the second column of Fig. 2. The cables are brighter in the LF image than in the images with higher frequencies. Since the cables are not parallel to the sonar path this may be caused by the fact that the LF sonar has observed the cables from a position where the acoustic signal hits the cables at a perpendicular angle.

A more complex frequency dependent effect is scattering. An example is vegetation that may have a very complicated frequency dependent scattering mechanism, depending on the size of the vegetation and whether it has air filled bladders. In the third column of Fig. 2, we show an example seabed, partly consisting of Posidonia and partly of sand. The image intensities are normalized such that the intensity of the parts with Posidonia is similar. Clearly, the echo from the sandy seafloor is much lower (relative to the Posidonia) for 72.5 kHz than for 300 kHz. Thus sandy seafloor reflects stronger at high frequencies and/or Posidonia reflects stronger at low frequencies (we cannot separate the two parts as long as we do not have calibrated sonars).

Another SAS specific frequency dependent effect is the image quality. Since the observation geometry is frequency dependent, the SAS processing is also dependent on frequency. This difference may affect the image quality in a number of ways, but the most obvious is the increased difficulty to navigate a longer synthetic aperture. At low frequencies the synthetic aperture is longer, and the navigation accuracy along the synthetic aperture has to be accurate within a fraction of a wavelength. Even though the absolute navigation restrictions are loosened for LF systems since the wavelength increases, this is insufficient to compensate for the increased difficulty in navigating the longer synthetic aperture. The result of an inaccurate navigation is blurring or defocus in the images. In the last column of Fig. 2, we can see that the LF image is blurred relative to the higher frequencies (this is most easily seen by the shadow fill-in).

5 STATISTICAL COMPARISON ON FLAT SEABED AND POSIDONIA

This section focuses on the comparison of the statistical distribution of pixels of a set of images of a flat sandy seabed and two sets of images of Posidonia. Each set of images is composed of two images obtained from the HUGIN-HUS system (i.e., HISAS LF and MF), as well as one image obtained from the MUSCLE system. REMUS100 data were not considered due to different geometry and coarser resolution. As visible in Table 1, for MUSCLE and HISAS the pixel resolutions of the different images are comparable along-track whilst the across-track resolution varies with frequency. The areas used in this initial study are those marked with a red square in Fig. 2. Histograms of the amplitudes normalized by the median value are calculated for each type of seabed and for each system for small homogeneous areas ($\sim$2x2 m) of the seabed illustrated by the red squares. These red boxes are for illustrative purposes only and do not necessarily reflect the exact size and location. However, within the analysis, care has been taken to ensure that the equivalent patch size on seafloor is taken for each system.

The histograms are subsequently normalized and the empirical cumulative distribution functions (cdf) are calculated. Current CMRE analysis suggests a gamma distribution to fit SAS amplitudes. Previous studies[20,21] have shown that SAS amplitudes may also be explained by K-law distributions in certain circumstances whilst some synthetic aperture radar data may be better modeled by a log-normal distribution[22,23]. Hence, we compare the data to these three distributions. Parameters of the gamma and log-normal distributions are estimated via a least means squares approach[24], whilst the K-law parameters are estimated using the method of moments[25].

A set of histograms and cdf's for the flat sandy area is shown in Fig. 3. MUSCLE and HISAS MF data present similar behaviors despite a difference in across-track resolution and frequency, i.e., long-tail distributions adequately fitted by a K-law distribution, whilst the low frequency and also across-track lower resolution present a more Rayleigh-like behavior. This would seem to suggest that despite the change in frequency and resolution between the MUSCLE and the middle frequency setup of HUGIN-HUS, the scattering phenomena are comparable whilst at the low frequency as well as the increase in across-track insonified patch size there may be some penetration into the seabed and therefore increasing the number of scatterers to a Rayleigh type distribution.

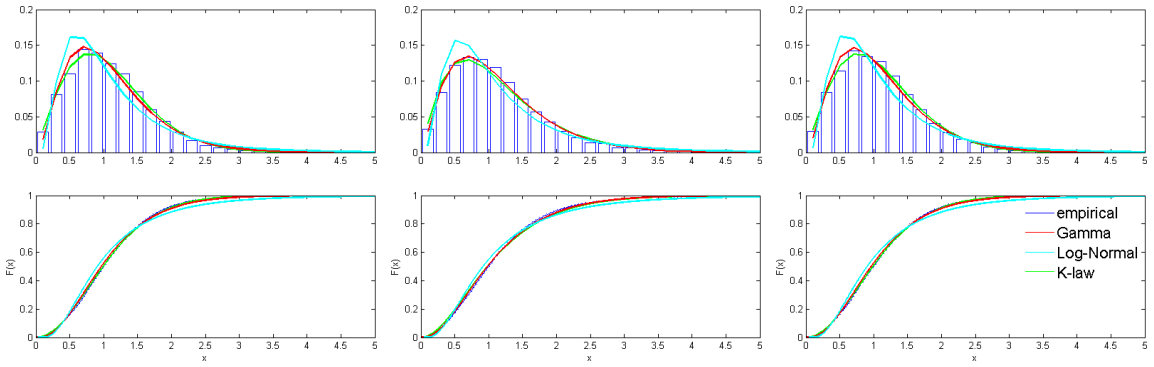

(a) HISAS LF **(b)** HISAS MF **(c)** MUSCLE

Figure 3: *Normalized histograms (top) and empirical cdf's (bottom) of same flat sandy seafloor area for the different systems and frequencies. Gamma distribution pdf's and cdf's are overlaid in red, log-normal in cyan and K-law in green.*

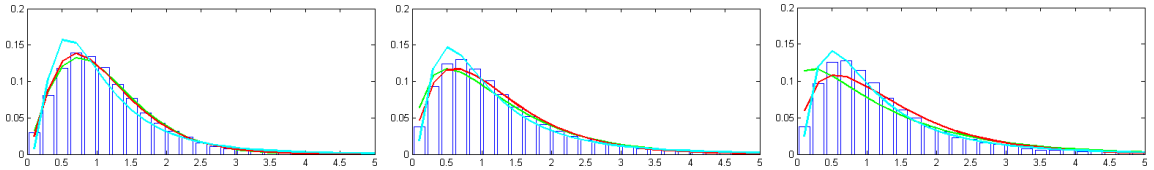

(a) HISAS LF **(b)** HISAS MF **(c)** MUSCLE

Figure 4: *Normalized histograms as in Fig. 3, but for first Posidonia area.*

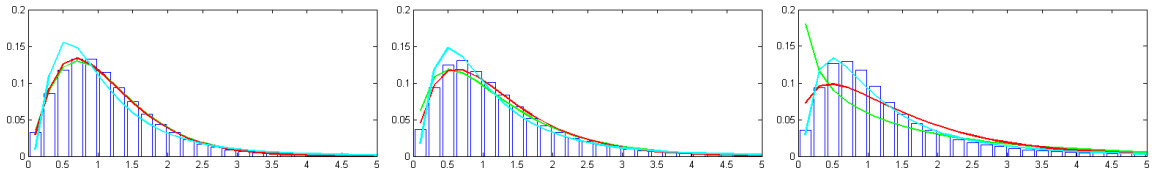

(a) HISAS LF **(b)** HISAS MF **(c)** MUSCLE

Figure 5: *Normalized histograms as in Fig. 3, but for dense Posidonia area.*

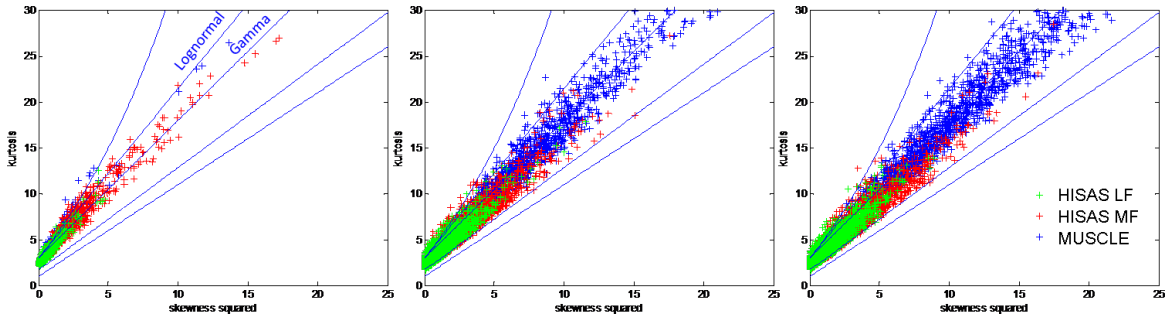

Figure 6: *Pearson diagrams for flat seabed (left), Posidonia (middle) and dense Posidonia (right). HISAS LF is in green, HISAS MF in red and MUSCLE data is in blue.*

Fig. 4 shows the normalized histograms and cdf's for the first example of Posidonia. It is interesting to note now that the behavior of the MUSCLE data starts to depart from that of the middle frequency HISAS data. The MUSCLE data can no longer be fitted with a single K-law distribution but is approaching a log-normal distribution and the tail is longer. The HUGIN-HUS data at both frequencies can still be fitted adequately with a K-law distribution.

This difference between systems and frequencies is accentuated for denser Posidonia as shown in Fig. 5. The MUSCLE data departs significantly from a K-law and a gamma distribution whilst converging towards a more log-normal behavior. The HISAS data at both frequencies displays a long-tail behavior with a gamma distribution adequately fitting the data. To understand if this is a general case or an exception, a larger area for each of the same seabeds was divided into blocks of 2x2 m. To visualize the variation of the distributions, the skewness squared versus kurtosis of each small block was plotted over a Pearson diagram[26]. These results are shown in Fig. 6. The behavior of the MUSCLE data on flat sandy seabed is comparable to the HISAS medium frequency data, and the HISAS low frequency data displays a less variable behavior with shorter tails. However, on Posidonia seabeds the center of gravity of the skewness squared/kurtosis couple is greatly increased for the MUSCLE data as well as the HISAS low frequency data for the first Posidonia example and for both HISAS frequencies for the denser Posidonia example. The results would also suggest that the data behavior fluctuates around a gamma distribution with some areas to be log-normally distributed.

Our preliminary study demonstrates some potential ideas for further environmental discrimination using multiple frequency or multiple resolution systems. We will continue this work with the aim of augmenting the in situ awareness for automatic target recognition and also for performance and evaluation purposes.

6 SUMMARY AND FUTURE WORK

We have presented, analyzed and discussed parts of a data set collected in a side experiment of MANEX'13 with multinational effort involving three different AUV systems and four carrier frequencies ranging from 18.5 to 900 kHz. This high-resolution imagery with large frequency disparity contributes to a better understanding of frequency dependent seafloor responses. Our efforts will continue for further investigation and collaboration on this interesting topic both for assessing seafloor and target properties. We plan to study the frequency dependent behavior of realistic mine objects and subsequently use information on the inner structure of an object, obtained from lower frequencies, to improve automatic target recognition (ATR) performance. Moreover, aspect angles differ with frequency, which may also provide useful information of object characteristics. Other future interests are to investigate seafloor penetration as function of frequency and grazing angle as well as how large frequency diversity can improve the characterization of the seafloor environment.

The frequency experiment provided us with valuable knowledge on which improvements are desired for a future measurements campaign aimed to take place at MANEX'14. We found out that the common waypoints were not set optimally. The distance between survey lines was too large such that the practical overlap for MUSCLE and HISAS data corresponded to a slant range interval of around 35 m. Apart from the waypoints, another reason to the small overlap is the reduced HISAS recording range due to gathering both LF and MF frequency bands simultaneously. It was less than half compared to two missions run with LF and MF one at a time. However, data acquisition in the combined mode lead to the advantage of well aligned SAS imagery not being exposed to any potential temporal effects. Further, several survey lines were located in rather shallow water of around 10 m depth close to the shore leading to multipath pollution, especially for the low frequencies. There was also severe acoustic interference in the LF band (26 – 38 kHz). It should be tried to be avoided in a future mission.

7 REFERENCES

1. M. Couillard, S. Dugelay, A. Grati, V. Djapic, O. J. Lorentzen, Ø. Midtgaard, T. Krogstad, R. van Vossen, A. Hunter, S. Giodini, A. Duijster, H. Dol, B. Quesson, M. Ditzel, B. Bakker, M. Zijlstra, J. Janssen, L. Kester, R. Naus, D. Bekers, and G. Beckers. MANEX'13: Summary and preliminary results, NATO STO-CMRE, Tech. Rep. CMRE-MR-2014-001. La Spezia, Italy (2014).

2. X. Lurton. *An Introduction to Underwater Acoustics: Principles and Applications*, 2nd ed. Springer Praxis Publishing. (2010).

3. R. E. Hansen. Introduction to Synthetic Aperture Sonar, in *Sonar Systems*, N. Z. Kolev (Ed.), InTech, Ch. 1, 3-28. (2011) .

4. D. Jackson and M. Richardson. *High-Frequency Seafloor Acoustics*, Springer-Verlag. (2007).

5. APL-UW High-Frequency Ocean Environmental Acoustics Models Handbook, Tech. Rep., Applied Physics Laboratory, University of Washington, Seattle, WA (1994).

6. K. L. Williams, S. G. Kargl, E. I. Thorsos, D. S. Burnett, J. L. Lopes, M. Zampolli, and P. L. Marston. 'Acoustic scattering from a solid aluminum cylinder in contact with a sand sediment: measurements, modeling, and interpretation', Journal of the Acoustical Society of America 127(6), 3356-3371. (June 2010).

7. T. M. Marston, P. L. Marston, and K. L. Williams. Scattering resonances, filtering with reversible SAS processing, and applications of quantitative ray theory, Proc. MTS/IEEE OCEANS 2010, 1-9. Seattle, WA (September 2010).

8. S. A. V. Synnes and R. E. Hansen. Ultra wideband SAS imaging, Proc. 1st International Conference and Exhibition on Underwater Acoustics, 111-118. Corfu, Greece (June 2013).

9. J. T. Christoff and J. E. Fernandez. Dual frequency synthetic aperture imaging sonar, Proc. Geoscience and Remote Sensing Symposium, Vol. 2, 624-626. Seattle, WA (July 1998).

10. D. A. Cook, J. T. Christoff, and J. E. Fernandez. Broadbeam multi-aspect synthetic aperture sonar, Proc. MTS/IEEE OCEANS 2001, Vol. 1, 188-192. Honolulu, HI (November 2001).

11. E. I. Thorsos, K. L. Williams, N. P. Chotiros, A. Member, J. T. Christoff, K. W. Commander, C. F. Greenlaw, D. V. Holliday, D. R. Jackson, J. L. Lopes, D. E. Mcgehee, J. E. Piper, M. D. Richardson, and D. Tang. 'An Overview of SAX99 : Acoustic Measurements', IEEE Journal of Oceanic Engineering 26(1), 4-25. (January 2001).

12. J. Christoff, J. Fernandez, and D. Cook. Unmanned underwater vehicle broadband synthetic aperture sonar, Proc. MTS/IEEE OCEANS'02, Vol. 3, 1871-1877. Biloxi, MS (October 2002).

13. J. E. Piper, R. Lim, E. I. Thorsos, and K. L. Williams. 'Buried sphere detection using a synthetic aperture sonar', IEEE Journal of Oceanic Engineering 34(4), 485-494. (October 2009).

14. J. E. Piper, K. W. Commander, E. I. Thorsos, and K. L. Williams. 'Detection of Buried Targets Using a Synthetic Aperture Sonar', IEEE Journal of Oceanic Engineering 27(3), 495-504. (July 2002).

15. S. G. Kargl, K. L. Williams, A. L. España, R. Lim, J. L. Kennedy, R. T. Arrieta, T. M. Marston, and J. L. Lopes. Synthetic Aperture Sonar (SAS) and Acoustic Templates for the Detection and Classification of Underwater Munitions, Proc. SERDP & ESTCP Annual Symposium. (2010).

16. J. D. Tucker and M. R. Azimi-Sadjadi. 'Coherence-Based Underwater Target Detection From Multiple Disparate Sonar Platforms', IEEE Journal of Oceanic Engineering 36(1), 38-52. (January 2011).

17. P. E. Hagen, T. G. Fossum, and R. E. Hansen. HISAS 1030: The Next Generation Mine Hunting Sonar for AUVs, Proc. UDT Pacific 2008. Sydney, Australia (November 2008).

18. A. Bellettini and M. A. Pinto, 'Design and Experimental Results of a 300-kHz Synthetic Aperture Sonar Optimized for Shallow-Water Operations', IEEE Journal of Oceanic Engineering 34(3), 285-293. (July 2009).

19. Sea Scan PC AUV Specifications, www.marinesonic.com. Accessed: 2014-07-18.

20. A. Hanssen, J. Kongsli, R. E. Hansen, and S. Chapman. Statistics of synthetic aperture sonar images, Proc. OCEANS 2003, Vol. 5, 2635-2640. San Diego, CA (September 2003).

21. S. Dugelay and V. Myers. A Correlated K-distributed Model for Seabed Reverberation in Synthetic Aperture Sonar Imagery, Proc. Institute of Acoustics, 163–168. (2010).

22. C. Oliver and S. Quegan. *Understanding Synthetic Aperture Radar Images*. SciTech Publishing, Inc., Raleigh, NC (2004).

23. V. Kerbaol, B. Chapron, and P. W. Vachon. 'Analysis of ERS-1/2 synthetic aperture radar wave mode imagettes', Journal of Geophysical Research 103(C4), 7833-7846. (April 1998).

24. G. J. Hahn and S. S. Shapiro. *Statistical Models in Engineering*, John Wiley & Sons Inc. (1994).

25. D. A. Abraham and A. P. Lyons. 'Reliable methods for estimating the K-distribution shape parameter', IEEE Journal of Oceanic Engineering 35(2), 288-302. (April 2010).

26. N. L. Johnson and S. Kotz. *Continuous Univariate Distributions, Volume 1*, John Wiley & Sons Inc., New York (1970).